ORIGINAL RESEARCH ARTICLE

In Situ Investigation of TCP Phase Formation, Stress Relaxation and γ/γ' Lattice Misfit Evolution in Fourth Generation Single Crystal Ni-Base Superalloys by X-Ray High Temperature Diffraction

A. BEZOLD, H.J. STONE, C.M.F. RAE, and S. NEUMEIER

In nickel-based superalloys, the lattice misfit between the γ and γ' phases and the propensity to TCP phase formation at service temperatures critically influence the microstructural evolution that takes place and hence the resultant mechanical properties. In this work, the lattice misfits of a series of highly alloyed Ru-containing 4th generation Ni-base superalloys are investigated by *in situ* X-ray diffraction (XRD) at high temperature. While the lattice misfit values of all alloys range between -0.3 and -1.3 pct at room temperature, they show an atypical temperature dependence, becoming less negative above 900 °C. *In situ* XRD measurements at 1100 °C reveal that the majority of the internal coherency stresses are already relieved after two hours. This is particularly pronounced for the alloys that have both a lattice misfit larger than $|0.6|$ pct at 1100 °C and are prone to TCP phase formation. However, throughout the relaxation of the internal coherency stresses the lattice misfit remains fairly constant. Due to the similar chemical compositions of the alloys studied, qualitative guidelines for an optimum lattice misfit magnitude are developed by comparing the lattice misfit values with previous creep experiments. Our results indicate that no universal optimal lattice misfit value exists for these alloys and the value strongly depends on the applied creep conditions.

Graphical Abstract
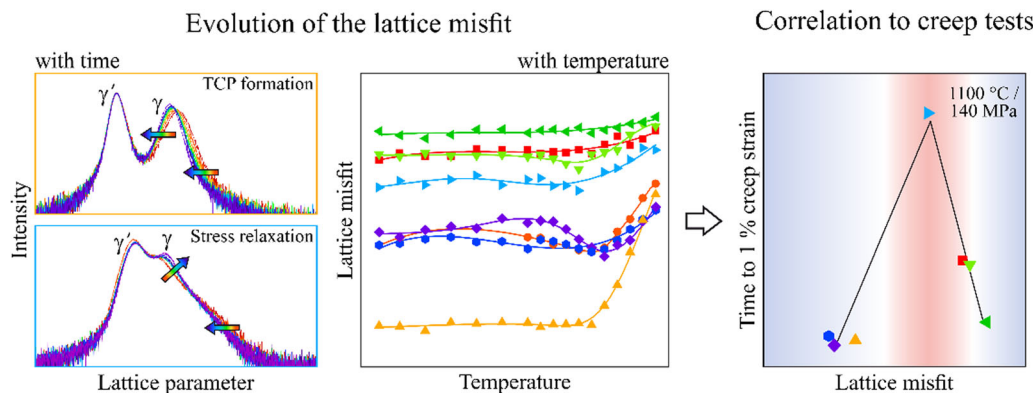
https://doi.org/10.1007/s11661-022-06713-2
© The Author(s) 2022

A. BEZOLD and S. NEUMEIER are with the Materials Science & Engineering, Institute I, Friedrich-Alexander-Universität Erlangen-Nürnberg (FAU), Martensstraße 5, 91058 Erlangen, Germany. Contact e-mail: steffen.neumeier@fau.de H.J. STONE and C.M.F. RAE are with the Department of Materials Science and Metallurgy, University of Cambridge, 27 Charles Babbage Road, Cambridge, CB3 0FS, UK.

I. INTRODUCTION

A key design requirement for commercial applications of single crystal nickel-based superalloys is excellent high temperature deformation resistance. This is commonly facilitated by alloy compositions containing significant concentrations of slowly diffusing refractory elements, such as Re, W, Mo and Ru. However, care is required to balance the concentration of these elements

to ensure that the desired microstructure of a solid solution fcc-γ matrix with coherently embedded and periodically aligned $L1_2$-γ' precipitates is maintained. In the high temperature regime ($T > 950$ °C), the stability of this optimally two-phase microstructure is threatened by numerous degradation processes: (i) formation of brittle, deleterious topological closed packed (TCP) phases, (ii) partial dissolution of the γ' phase, (iii) loss of coherency between the γ' precipitates and the γ matrix and (iv) (directional) coarsening of the γ' precipitates.

For the last two points, the sign and magnitude of the relative difference between the lattice parameters of the γ and γ' phases (a_γ and $a_{\gamma'}$) in the alloy plays an important role. This so-called constrained γ/γ' lattice misfit is defined as follows:

$$\delta = \frac{a_{\gamma'} - a_\gamma}{0.5(a_{\gamma'} + a_\gamma)} \qquad [1]$$

For a non-zero lattice misfit, coherency stresses arise in both the γ and the γ' phases leading to the characteristic cuboidal γ' precipitate shape, which is considered to be optimal for a lattice misfit of about $\pm$ 0.4 pct.[1] If the magnitude is lower or higher, the shape of the precipitates becomes more globular or the coherency between the phases is lost, respectively.[1] While higher lattice misfit magnitudes have been strongly correlated to increased room temperature hardness values,[2] an optimal value of the lattice misfit for maximum creep strength is still under debate.[3] For many service applications, a smaller lattice misfit is considered beneficial due to reduced coarsening rates and a higher microstructural stability.[4] In contrast, denser interfacial networks caused by higher lattice misfit values are reported to increase the creep resistance by impeding shearing processes.[5,6] However, denser interfacial networks also accelerate the partial dissolution of the γ' precipitates.[7] Simulations by Svoboda and Lukas[8] revealed that a higher lattice misfit improves the creep properties in the low temperature/high stress regime (*e.g.* 750 °C/800 MPa) by impeding primary creep, while a lower lattice misfit is beneficial in the high temperature/low stress regime (*e.g.* 1000 °C/150 MPa). Such an evolution of the lattice misfit typically does not occur in commercial 1st and 2nd generation Ni-base superalloys as these alloys typically have lattice misfits that are close to zero and become more negative with increasing temperature.[9,10] Interestingly, novel γ–γ' Co-base superalloys,[11,12] as well as some 4th generation Ni-base superalloys with high enough Re and Ru contents,[13,14] also exhibit the above-mentioned favorable temperature dependence of the lattice misfit.

In the latest 4th generation of Ni-base superalloys, Ru was added to improve the microstructural stability.[15–20] However, even with these additions, excessive contents of refractory elements still promote the formation of TCP phases, such as the σ, P and μ phases.[19,21,22] These phases cause a decrease of the creep strength as they are strongly enriched with refractory elements and their formation consequently depletes the γ matrix of these elements.[20,23] The occurrence of these phases is also associated with an increase in the susceptibility of an alloy to crack initiation and propagation as a result of their high elastic moduli and low toughnesses.[22,24,25]

Numerous previous studies have investigated the evolution of the lattice misfit from the as-aged condition to the creep deformed state.[26–30] However, the microstructure changes considerably after heating the sample above the last aging temperature. Thus, it is of fundamental importance to understand how the microstructure evolves during short-term aging at high temperatures and how this affects the lattice misfit if the corresponding creep response at the same temperature is to be rationalized. In this work, X-ray diffraction is used to study the (002) reflections of three different alloys as a function of time at 1100 °C to investigate the influence of TCP phase formation, the effect of stress relaxation, and the combination of both. Additionally, the lattice misfit is determined as a function of temperature for eight 4th generation Ni-base superalloys that cover a wide range of possible negative lattice misfit values ($-$ 0.3 to $-$ 1.3 pct). Combined with the information from the *in situ* aging experiments, the lattice misfit values obtained are subsequently correlated to previously published creep results[31] for all three creep regimes exhibited by advanced Ni-base superalloys.

II. EXPERIMENTAL METHODS

The investigated LDSX alloy series was created using a design of experiment approach to study the influence of Co, Ru, Mo and W on the microstructure and properties of 4th generation Ni-base superalloys.[31] Eight 4th generation Ni-base superalloys with varying amounts of Co, Mo, Ru and W (see Table I) were cast as single crystalline bars at the Precision Casting Facility (PCF) in Rolls-Royce plc, Derby, UK. The subsequent heat treatment procedure consisted of a solutionizing and homogenization step between 1340 °C and 1365 °C for 10 to 20 hours. According to EPMA (electron probe microanalysis) measurements, this reduces the segregation, *i.e.* the concentration ratio between dendrite cores and interdendritic regions, of the strongest segregating element, Re in LDSX-2, for example, from about 7.1 down to 1.4. Afterwards, the alloys were subjected to a primary γ' precipitate age of 4 hours at 1150 °C, followed by a secondary γ' precipitate age of 16 hours at 870 °C.

After mechanical grinding to 100 μm thin discs and electropolishing at $-$ 5 °C and 25 V with a solution of 10 pct perchloric acid in methanol, foils of all investigated LDSX alloys in the as heat-treated condition were characterized using a JEOL 200CX transmission electron microscope (TEM). The edge length of the primary γ' precipitates and the γ' volume fraction were determined by ImageJ[32] using the procedure introduced in Reference 33. After short-duration aging at 1100 °C for 60 or 180 minutes, the microstructural changes that occurred in LDSX-3, LDSX-6 and LDSX-8, compared with the as heat-treated state, were investigated using a Philips XL-30 Field Emission Gun Scanning Electron Microscope (FEGSEM).

Table I. Nominal Composition of the Single Crystalline Ni-Base Superalloys LDSX-1 to -8

		Ni	Cr	Co	Mo	W	Ru	Re	Al	Ti	Ta	Hf
LDSX-1	wt pct	bal.	3.0	3.0	2.5	2.9	3.5	6.2	6.0	0.25	6.5	0.1
	at. pct	bal.	3.6	3.2	1.6	1.0	2.2	2.1	13.8	0.32	2.2	0.03
LDSX-2	wt pct	bal.	3.0	8.0	5.0	2.9	3.5	6.2	6.0	0.25	6.5	0.1
	at. pct	bal.	3.6	8.5	3.3	1.0	2.2	2.1	14.0	0.33	2.3	0.04
LDSX-3	wt pct	bal.	3.0	3.0	5.0	4.8	3.5	6.2	6.0	0.25	6.5	0.1
	at. pct	bal.	3.7	3.2	3.3	1.7	2.2	2.1	14.2	0.33	2.3	0.04
LDSX-4	wt pct	bal.	3.0	8.0	2.5	4.8	3.5	6.2	6.0	0.25	6.5	0.1
	at. pct	bal.	3.6	8.6	1.6	1.7	2.2	2.1	14.0	0.33	2.3	0.04
LDSX-5	wt pct	bal.	3.0	8.0	2.5	2.9	5.0	6.2	6.0	0.25	6.5	0.1
	at. pct	bal.	3.6	8.5	1.6	1.0	3.1	2.1	13.9	0.33	2.3	0.04
LDSX-6	wt pct	bal.	3.0	3.0	2.5	4.8	5.0	6.2	6.0	0.25	6.5	0.10
	at. pct	Bal.	3.7	3.2	1.6	1.7	3.1	2.1	14.1	0.33	2.3	0.04
LDSX-7	wt pct	bal.	3.0	3.0	5.0	2.9	5.0	6.2	6.0	0.25	6.5	0.10
	at. pct	bal.	3.7	3.2	3.3	1.0	3.1	2.1	14.1	0.33	2.3	0.04
LDSX-8	wt pct	bal.	3.0	8.0	5.0	4.8	5.0	6.2	6.0	0.25	6.5	0.10
	at. pct	bal.	3.7	8.7	3.3	1.7	3.2	2.1	14.3	0.34	2.3	0.04

The evolution of the (002) reflections for all LDSX alloys was investigated by X-ray diffraction (with Cu-K$_{\alpha 1}$ radiation) using a special double-crystal diffractometer, which has negligible instrumental peak broadening and high angular resolution.[26,34] The (001)-oriented samples, which had a thickness of 0.5 to 1.0 mm, were heated in vacuum between RT and 1100 °C using an *Anton Paar HTK 10* high temperature chamber. Line scans through the (002) fundamental reflections were obtained at RT and after the step-wise heating to the respective target temperature and holding it there for 5 minutes at each temperature (100 °C, 200 °C, 300 °C, 400 °C, 500 °C, 600 °C, 650 °C, 700 °C, 750 C, 800 °C, 850 C, 900 °C, 950 °C, 1000 °C, 1050 °C and 1100 °C). After the samples reached 600 °C, the temperature was held constant for another 30 minutes in order to crystallize the water glass, which was used for fixing the thin samples on the heating band, before the temperature was increased to the next target temperature. Accordingly, the total duration of these *in situ* heating experiments was about 3 hours per sample. After the final temperature of 1100 °C was attained further line scans were recorded after 5 to 180 minutes for LDSX-3, LDSX-6 and LDSX-8.

The (002) diffraction peak profiles were fitted with three Pseudo-Voigt functions, one for the γ' phase, and two for the γ phase to account for the tetragonal distortion of the γ matrix that arises as a result of the coherency stresses and gives rise to different lattice spacings in the [001] direction of the vertical and horizontal γ matrix channels.[14] The volume of the γ matrix channels parallel to the [001] direction (vertical γ channels) is twice as large as that of the γ matrix channels, which are perpendicular to the [001] directions (horizontal γ channels). Thus, the ratio of the areas of the fitted sub-peaks was set to 2:1 ($\pm$ 15 pct tolerated deviation). In order to subsequently calculate the γ/γ' lattice misfit with Eq. [1], the equivalent cubic γ lattice parameter, a_{cub}, was determined using the equation[35]:

$$a_{\text{cub}} = \frac{(1 - v)a_{\gamma,\text{h}} + 2va_{\gamma,\text{v}}}{1 + v}, \qquad [2]$$

where $a_{\gamma,\text{v}}$ and $a_{\gamma,\text{h}}$ are the lattice parameters of the vertical and horizontal γ channels and v is the Poisson ratio. Since the Poisson ratios for the matrices of the different LDSX alloys have not been previously determined, the temperature dependent Poisson ratios of the matrix of CMSX-4 from the work of Siebörger et al.[36] were used. For more details on the fitting procedure and the different approaches to determine the γ lattice parameter and γ/γ' lattice misfit, the reader is referred to the study of Neumeier et al.[14]

III. RESULTS

A. *As Heat-Treated Microstructure*

TEM micrographs of the dendritic cores of the investigated LDSX alloys after aging are shown in Figure 1. As previously reported,[31] the γ' precipitates in LDSX-8 directionally coalesce to form so-called pre-rafts. Some of the γ' precipitates have partially grown together along the $\langle 001 \rangle$ directions and are separated just by thin remaining γ channels. Nevertheless, most of the γ' precipitates can still be considered as cuboidal. Secondary γ' precipitates were observed in the wider γ channels in LDSX-1, LDSX-4, LDSX-6 and LDSX-8 (see Figures 1(a), (d), (f), (h)), having not been eliminated by the secondary precipitate age. In LDSX-2 and LDSX-3, TCP phases were observed to have already formed after the aging steps, as shown in Figures 1(b) and (c). Additionally, the numerous interfacial dislocations in the microstructure of LDSX-3 reveal that the coherency between the γ matrix and the γ' precipitates in this alloy is already partly lost, suggesting that the absolute value of the lattice misfit in LDSX-3 is higher than in the other investigated LDSX alloys. As shown in Table II, the γ' edge lengths and γ' volume fractions are
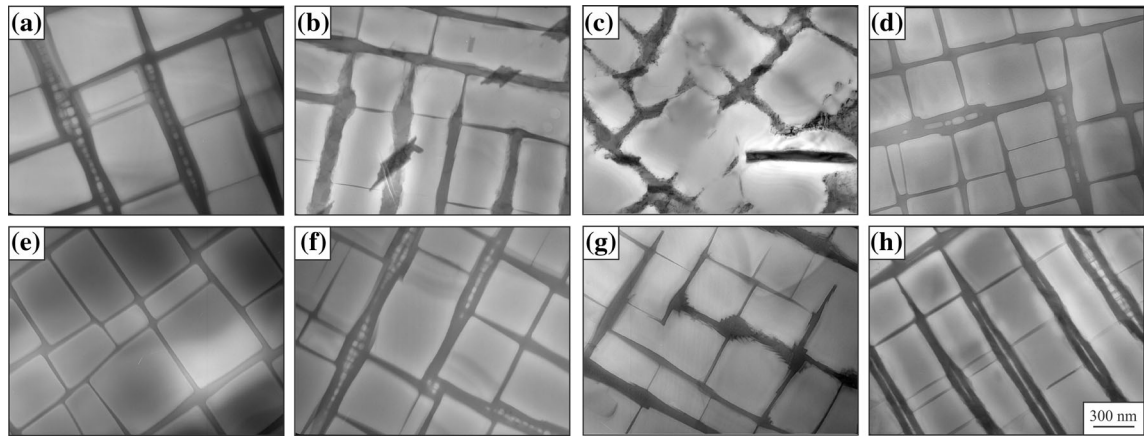
Fig. 1—As-aged microstructures of the alloys (*a*) LDSX-1, (*b*) LDSX-2, (*c*) LDSX-3, (*d*) LDSX-4, (*e*) LDSX-5, (*f*) LDSX-6, (*g*) LDSX-7 and (*h*) LDSX-8. TCP phases are already precipitated in LDSX-2 and LDSX-3.

similar in all eight LDSX alloys, ranging from 339 to 435 nm and 61 to 73 pct, respectively. Only LDSX-3 exhibits a slightly larger γ' edge length of 504 nm, presumably due to the semi-coherency of the matrix-precipitate interface in the as-aged condition.

Despite the homogenization heat treatment, residual solidification-induced segregation is still present, leading to small differences in the γ' precipitate size and volume fraction between the dendritic and interdendritic regions. While these variations can also influence the lattice parameters of both phases and the resulting lattice misfit,[37–39] our previous study on the LDSX alloy series demonstrated that the peak shapes arise predominantly due to the γ/γ' microstructure and the present internal coherency stresses and not due to segregations on the dendritic scale by comparing LDSX-2 and LDSX-4.[40] Although LDSX-4 has a stronger residual segregation on the dendrite scale due to the higher W concentration, LDSX-2 showed more pronounced subpeaks due to the higher Mo content, which partitions more strongly to the γ phase and hence leads to a greater tetragonal distortion of the γ unit cell.[40] Additionally, we will show in another subsequent publication in more detail how the individual features of the γ/γ' microstructure contribute to the characteristic peak shapes and that they arise predominantly due to the present internal coherency stresses and not due to segregations on the dendritic scale. Thus, the influence of these chemical heterogeneities are minor and only briefly considered in the following analyses.

B. *Lattice Misfit as a Function of Temperature*

To determine the lattice parameters of the γ and γ' phases, XRD data was acquired as a function of the temperature, T. Examples of the (002) reflections obtained from three LDSX alloys—LDSX-3, LDSX-6 and LDSX-8—at room temperature and 1100 °C are shown in Figure 2. For each of these plots, the raw data are shown by open symbols and the fitted subpeaks are identified by solid lines. As has been reported in a previous study,[40] the room temperature XRD line profile of LDSX-3 could not be fitted adequately by three Pseudo-Voigt functions (see Figure 2(a)).

It should be noted that the peak asymmetries that are not accounted for with these fits cannot be attributed to elemental segregation on the dendritic scale or other effects. Rather, they are due to the distortion of the γ matrix phase, as will be analyzed in detail in a forthcoming paper as these effects are beyond the scope of the current work.

Due to the low volume fraction of the secondary γ' precipitates (see Figures 1(a), (d), (f), (h)), their influence on the (002) reflections can be considered to be minor. Thus, only a single γ' peak was fitted, which include the contribution from the secondary γ' precipitates. Both of the peaks that are attributed to the vertical and horizontal channels of the γ matrix phase are much broader due to the larger lattice parameter distribution arising from varying γ channel widths, γ channel crossings, etc. In contrast to LDSX-3, only two peaks can be distinguished in the (002) reflection from LDSX-6 at room temperature, implying that this alloy has a smaller lattice misfit (see Figure 2(b)). The line profile of LDSX-8 reveals that the magnitude of its lattice misfit is larger than that of LDSX-6, but smaller than that of LDSX-3 as shown in Figure 2(c). At 1100 °C, the peaks of γ and γ' are clearly separated in LDSX-3 and the γ subpeak is fairly symmetric (see Figure 2(d)). This observation is consistent with the residual coherency stresses being relieved and coherency being lost between both phases. Besides, this symmetry of the γ subpeak provides clear evidence that a residual segregation on the dendrite scale is not the origin of the asymmetry of the γ subpeak at lower temperatures. The residual segregation does not vanish at such low temperatures and short heating durations of this *in situ* measurement compared to the solution heat treatment and should also lead to an asymmetry at 1100 °C, if it was the reason. The distorted (002) reflection at 1100 °C in Figure 2(e) suggests that the lower lattice misfit in LDSX-6 allows the γ' precipitates to remain coherently (or at least semi-coherently) embedded in the γ matrix. Similar to LDSX-3, two distinctive peaks are observed

Table II. γ′ Edge Length and Volume Fraction of the LDSX Alloys in the As-Aged Condition Determined by the Method Introduced in Ref. [33]

	LDSX-1	LDSX-2	LDSX-3	LDSX-4	LDSX-5	LDSX-6	LDSX-7	LDSX-8
γ′ Edge Length/nm	393 ± 103	435 ± 82	504 ± 140	365 ± 81	388 ± 85	397 ±108	339 ± 95	353 ± 77
γ′ Vol. Frac./Pct	67 ± 2	61 ± 3	68 ± 2	73 ± 6	68 ± 3	68 ± 1	67 ± 3	69 ± 3

For the calculation of the γ′ edge length, secondary γ′ precipitates were not considered.
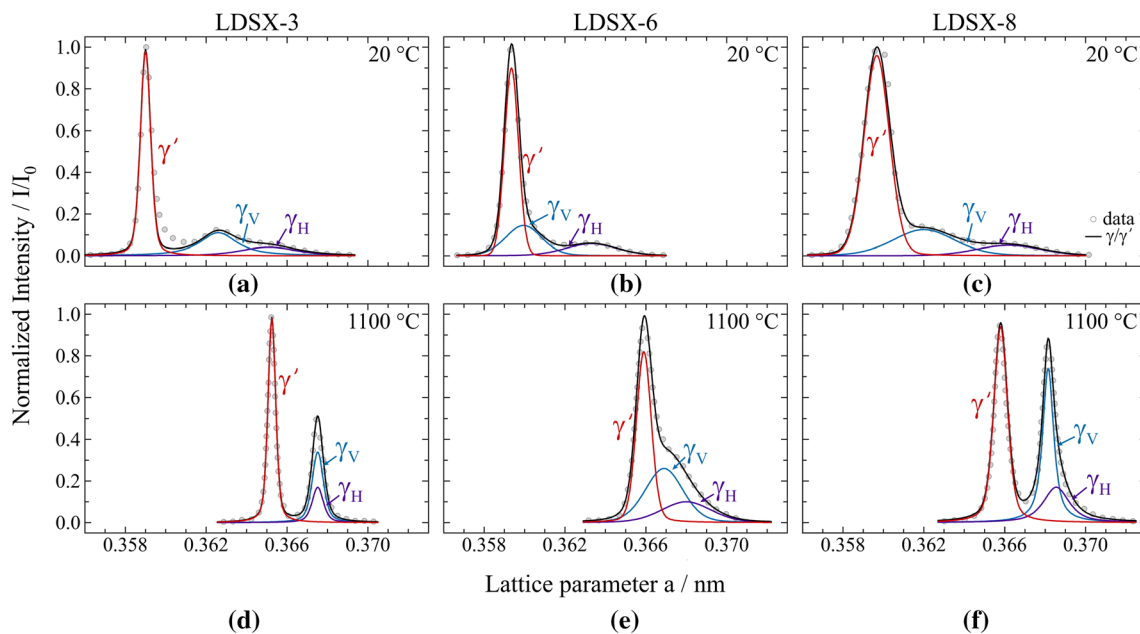
Fig. 2—Measured (002) reflections of (a, d) LDSX-3, (b, e) LDSX-6 and (c, f) LDSX-8 at (a through c) room temperature (20 °C) and (d through f) 1100 °C. The overall fit (black line) to the measured data points (grey circles) consists of three subpeaks arising from the γ′ precipitates (red line) and the vertical and horizontal γ channels ($γ_v$ and $γ_h$, respectively) (Color figure online).

for LDSX-8 as shown in Figure 2(f). The convergence of the peaks associated with the γ phase indicates that the coherency between both phases is reduced following exposure at 1100 °C. However, the γ peak retains some asymmetric distortion due to the different peak positions of the vertical and horizontal γ subpeaks, which implies that coherency stresses are still acting at this condition. Thus, coherency is not completely lost and the γ matrix is still partially tetragonally distorted.

The lattice misfit as a function of the temperature of all of the LDSX alloys investigated shows an atypical behavior: instead of getting more negative with increasing temperature, the magnitude of the lattice misfit decreases and gets closer to 0, as shown in Figure 3.

Recently, Neumeier et al.[14] observed that this atypical behavior occurs in Ni-base superalloys with a combined Re and Ru concentration greater than 4 at. pct, i.e. for 4th generation Ni-base superalloys as in this study. While the magnitude of the lattice misfit of LDSX-2, LDSX-4, LDSX-6, and in particular LDSX8, increases between 650 °C and 900 °C, it decreases again at higher temperatures. The intermediate increase is believed to occur as a result of the larger thermal expansion coefficient of the γ phase compared to that of the γ′ phase, however, this effect may also arise from precipitation of secondary γ′ precipitates. Such
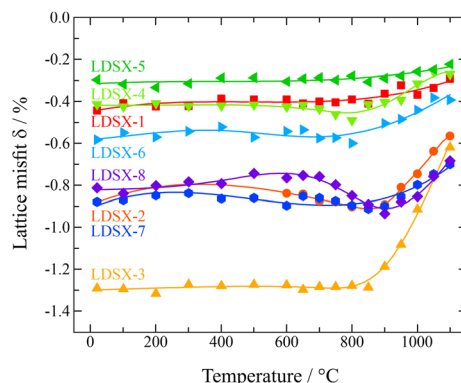

Fig. 3—Lattice misfits of the investigated LDSX alloys as a function of the temperature.

precipitates may form in the temperature regime between 650 °C and 870 °C, which was the final aging temperature. As a result, the γ phase became richer in γ forming elements, such as Mo, Re and Ru, and its lattice parameter would get even larger and the lattice misfit more negative. The subsequent decrease up to 1100 °C, which occurs in all alloys, is attributed particularly to the change in the chemical composition of the γ′ and especially the γ phase as a result of the γ′ dissolution and

elemental partitioning and not to the different thermal expansion coefficients of both phases.[14] Interestingly, the decrease of the lattice misfit magnitude between 850 °C and 1100 °C seems to increase with the magnitude of the room temperature misfit value, *i.e.* the decrease is smaller/higher for lower/higher negative lattice misfit values.

The slight differences between the RT lattice misfits determined in Reference 40 and in this study are mainly due to the different approach used in Reference 40 to determine the γ lattice parameter and γ/γ′ lattice misfit. For further information on the different approaches, the reader is referred to Reference 14.

C. *In Situ XRD Measurements and Microstructural Evolution at 1100 °C*

To investigate the influence of TCP phase formation and/or the relaxation of coherency stresses, the temporal evolution (between 15 and 180 minutes) of the (002) reflections of LDSX-3, LDSX-6 and LDSX-8 was investigated at 1100 °C, as shown in Figure 4. The individual reflections at each time step were again fitted with three Pseudo-Voigt functions. The evolution of the fitted lattice parameters of the γ′ precipitates as well as the vertical and horizontal γ channels for these three LDSX alloys are shown in Figure 5.

In LDSX-3, the γ′ subpeak at smaller lattice parameters remains constant, while the combined γ matrix peak shifts to lower lattice parameter values with increasing time at temperature (see Figure 4(a)). Additionally, the width of the γ peak decreases and gets more symmetrical, as confirmed by the fitted lattice parameters shown in Figure 5(a). The lattice parameters of both γ subpeaks decrease and converge at 60 minutes, which implies that any residual coherency is completely lost at this point. The reason for the decrease of the lattice parameter of the γ phase is the formation of TCP phases—in the case of LDSX-3 the formation of the σ

and *P* phases.[21] Since the σ, *P* and other TCP phases are enriched in refractory elements (Mo, Re, W),[17,20,23] the γ matrix is consequently depleted by these elements. Due to their higher atomic radii in comparison to Ni,[41] their depletion leads to the observed reduction of the γ lattice parameter. The significant formation of the TCP phases after 60 minutes at 1100 °C is also confirmed by SEM investigations in comparison to the standard heat-treated condition, as shown in Figures 6(a) and (d). In these images, the TCP phases exhibit bright contrast in the back-scattered electron imaging mode used due to the higher average atomic mass of these phases.

In LDSX-6, the peak of the γ′ phase evolves to slightly higher lattice parameters during exposure at 1100 °C, while the γ subpeak becomes more symmetrical and develops from a shoulder on the γ′ reflection to a clearly distinguishable peak (see Figure 4(b)). These observations indicate that the coherency stresses are relieved and the lattice parameter in the same crystallographic direction of the vertical γ channels increases, while that of the horizontal γ channels decreases, as shown in Figure 5(b). Microstructural examination of LDSX-6 following the standard heat treatment (Figure 6(b)) and after an additional *ex situ* exposure for 180 minutes at 1100 °C (Figure 6(e)), revealed that no other third phases precipitated. As such, the change of the peak shape can be solely attributed to the relaxation of the coherency stresses. Even after a prolonged aging time of 750 hours, only a small amount of TCP phases formed in this alloy (inset in Figure 6(e)). However, the edges of the γ′ precipitates become more irregular, indicating that the remaining coherency stresses in LDSX-6 after aging for 180 minutes at 1100 °C are partly relieved after this longer duration aging.

LDSX-8 represents an intermediate scenario between LDSX-3 and LDSX-6. While the formation of TCP phases in LDSX-3 and the relaxation of the coherency stress in LDSX-6 are the dominant processes influencing
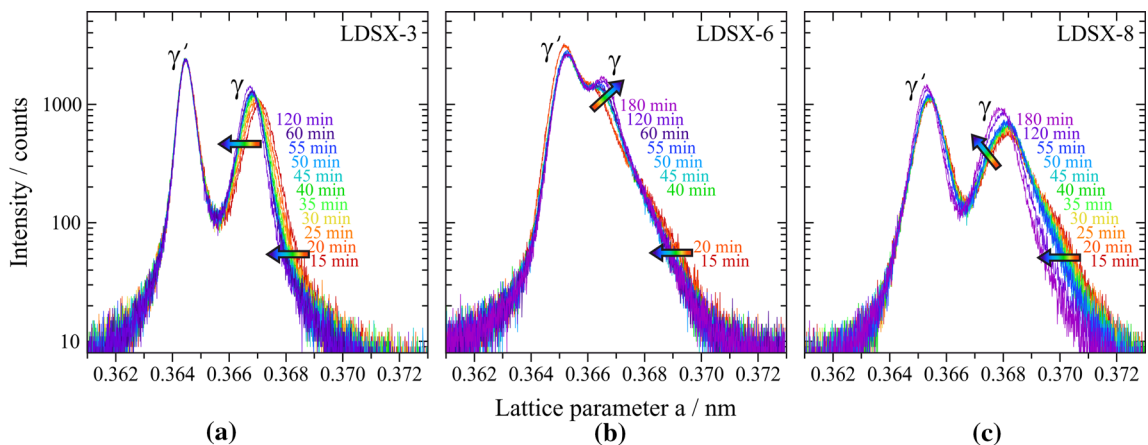

Fig. 4—Temporal evolution of the (002) reflections of (*a*) LDSX-3, (*b*) LDSX-6 and (*c*) LDSX-8 recorded during the *in situ* heating experiments at 1100 °C.
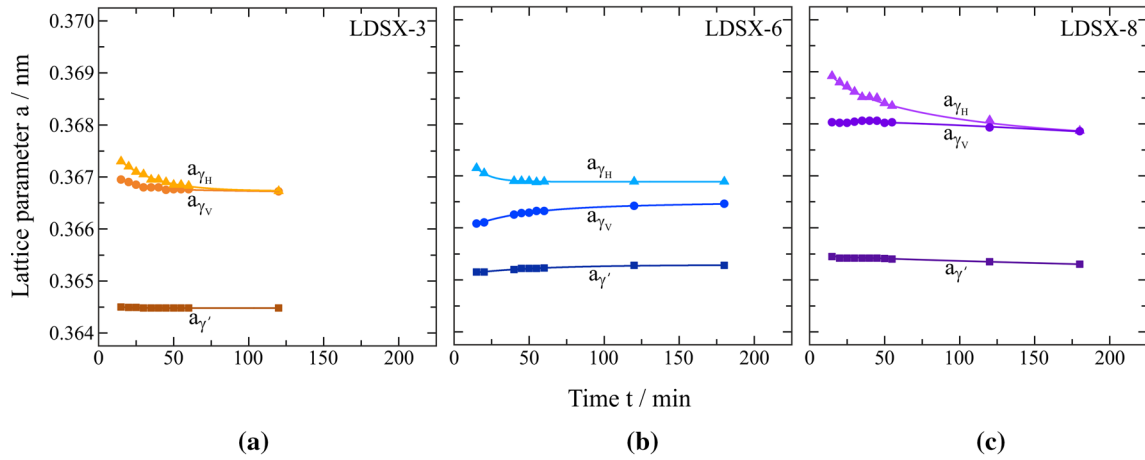
Fig. 5—Temporal evolution of the lattice parameter of the γ' phase as well as the horizontal and vertical channels of the γ phase of (*a*) LDSX-3, (*b*) LDSX-6 and (*c*) LDSX-8 during the *in situ* heating experiments at 1100 °C.
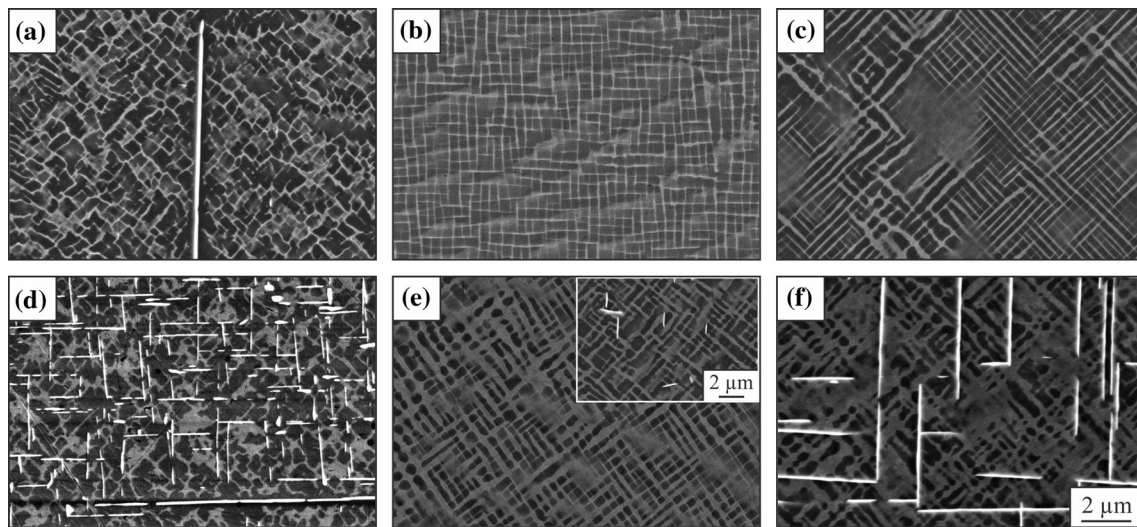

Fig. 6—Back scattered electron images of the microstructures in the (*a*) through (*c*) as heat-treated condition and (*d*) through (*f*) after heating at 1100 °C for (d) 60 min, (e) 180 min and (f) 180 min. (a, d) LDSX-3, (b), (e) LDSX-6 and (c, f) LDSX-8. The inset of (e) shows the microstructure of LDSX 6 after annealing for 750 h at 1100 °C.

the evolution of the (002) reflections, both processes play a major role in the aging of LDSX-8. In the X-ray data acquired from this alloy, the shoulder of the γ subpeak corresponding to the horizontal γ channels shifts appreciably to lower lattice parameters (see Figure 5(c)). In contrast to LDSX-6, the subpeaks of the vertical γ channels and the γ' precipitates also decrease to lower lattice parameters and the overall γ subpeak becomes more symmetrical. The evolution of the fitted lattice parameter confirms these observations and additionally reveals that the lattice parameters of both γ channel types converge after approximately 120 minutes, as shown in Figure 5(c). During this aging treatment, TCP phases are precipitated, which are absent in the standard heat-treated condition (see Figures 6(c) and (f)). Again, these TCP phases are enriched in heavy refractory elements and thus, lead to the observed reduction of the lattice parameter of the γ matrix phase.

IV. DISCUSSION

Even though the maximum service temperature of advanced single crystalline Ni-base superalloys is significantly above 1000 °C, the temperature of the last step of the aging heat treatment is usually in the range of 850 °C to 900 °C. Thus, subsequent measurements of the lattice misfit and the remaining coherency stresses in the as-aged microstructure at room temperature do not reveal the true internal stress state at the operating temperature. Furthermore, the γ/γ' microstructure evolves at these higher temperatures. Besides the different thermal expansion of both phases, microstructural changes including the partial dissolution of the γ' phase, the precipitation of TCP phases and/or the relaxation of the coherency stresses occur and change both the lattice misfit and the coherency stresses. These microstructural changes also cause the atypical evolution of the lattice misfit with increasing temperature due to the dissolution

of the γ′ phase and the changing chemical compositions of the γ and γ′ phase, in particular the dilution of Re and Ru in the γ matrix.[14]

A. Coherency Stress Evolution at 1100 °C

Using the fitted lattice parameters of the *in situ* XRD measurements shown in Figure 5, the lattice misfits and the remaining coherency stresses in the γ matrices can be calculated. As shown in Figure 7(a), the lattice misfit remains approximately constant for LDSX-6, while its magnitude decreases steadily for LDSX-3 and LDSX-8. Since the lattice misfit is calculated by the equivalent cubic lattice parameter, the influence of coherency stresses on the evolution of the lattice misfit is negligible. This difference in behavior can be attributed to the formation of the TCP phases, which are strongly enriched in refractory elements. As they form, the lattice parameters of the γ matrix and thus also that of the cubic equivalent lattice parameter become smaller, explaining the observed decrease of the magnitude of the lattice misfit of LDSX-3 and LDSX-6. Since no TCP formation is observed in LDSX-6 after short-term aging at 1100 °C, as confirmed by the SEM investigations in Figure 6(d), the lattice parameter of the γ matrix and thus the γ/γ′ lattice misfit remain constant.

While the coherency stresses in the matrix are usually assumed to be proportional to the lattice misfit, this is only true, if the phase boundaries are still completely coherent. The coherency stresses are related to the tetragonal distortion of the γ matrix channels, which is defined as the ratio of the lattice parameters of the vertical and horizontal γ channels. After Zenk *et al.*, the coherency stress σ_{coh} along the γ/γ′ interfaces can be estimated as follows[35]:

$$\sigma_{\mathrm{coh}} = \frac{E_{[001]}}{1-v}\left(\frac{a_{\gamma,\mathrm{h}} - a_{\gamma,\mathrm{cub}}}{a_{\gamma,\mathrm{cub}}}\right), \qquad [3]$$

where $E_{[001]}$ is the Young's modulus in the [001] direction and v is the Poisson ratio. Inserting the extrapolated values at 1100 °C of the pure matrix phase of CMSX-4 from the work of Siebörger *et al.*[36] yields $E_{[001]} = 69$ GPa and $v = 0.42$. The evolution of the calculated coherency stresses is shown in Figure 7(b). Given the observation of interfacial dislocation networks after the standard heat treatment in LDSX-3, the comparatively low initial coherency stresses of 70 MPa in this alloy is not surprising. Consistent with the convergence of the lattice parameters of the vertical and horizontal γ channels, the coherency stresses approach 0 MPa after 120 minutes at 1100 °C. Although the initial coherency stresses at 1100 °C in LDSX-8 are nearly as high as in LDSX-6, they decrease substantially and also converge to 0 MPa after 180 minutes. The higher microstructural stability of LDSX-6, as also shown in Figure 6(e), is also evident. In contrast to the other two alloys, the coherency stresses in this alloy are not completely relieved and only partially relaxed to approximately 85 MPa after 180 minutes. These observations further emphasize that the correlation of the lattice misfit with the acting coherency stresses is insufficient if coherency is partially lost. In this case, the tetragonal distortion of the matrix is the only relevant parameter to calculate the coherency stresses.

B. Implications for Creep Properties

The deformation behavior of advanced single crystal Ni-base superalloys strongly depends on temperature and stress. Based on the underlying deformation mechanisms, the creep behavior is usually distinguished in three different regimes: low temperature/high stress (LTHS) (*e.g.* 750 °C/800 MPa), intermediate temperature/stress (ITIS) (*e.g.* 950 °C/350 MPa) and high temperature/low stress (HTLS) (*e.g.* 1100 °C/140 MPa). While optimum values for the γ′ size and γ′ volume fraction have already been experimentally determined,[42–44] an optimum value of the lattice misfit is still debated.[3] Since the lattice misfit strongly depends on the chemical composition of the alloy, it is difficult to isolate its influence on the overall creep strength.

Despite these difficulties, the alloys studied in this work exhibit similar γ′ volume fractions and γ′ precipitate sizes and only change their composition in regards to their Co, Mo, W and Ru content. The content of the potent solid solution strengthening elements Mo and W varies between 2.6 and 5.0 at. pct throughout the alloy series. We are aware that these differences play an important role and the differences in the lattice misfits are not the sole and maybe not the dominant factor that
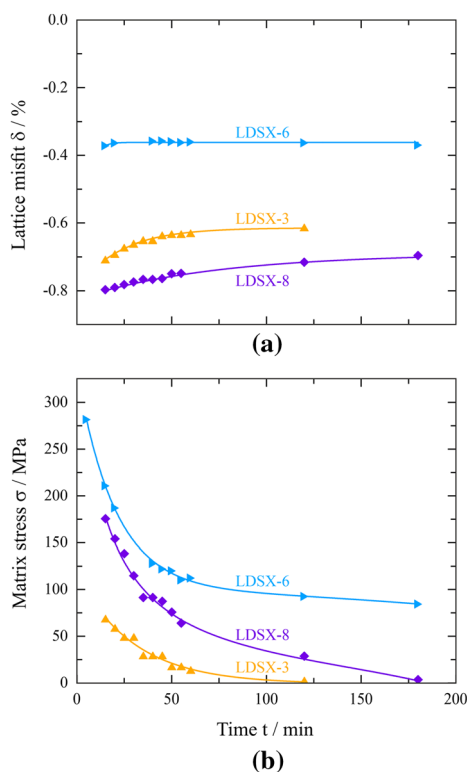

Fig. 7—Evolution of (*a*) the lattice misfit and (*b*) the remaining coherency stress in the γ matrix channels in LDSX-3, LDSX-6 and LDSX-8 as a function of time at 1100 °C.

governs the creep properties, however, the correlation of the measured high temperature lattice misfit values at the respective temperatures with the previously determined creep strength of these alloys[31] provides an opportunity to qualitatively study the influence of the lattice misfit in the different creep regimes. Even though some degree of data scattering can be expected due to the differences in the chemical composition, which results in different degrees of solid solution strengthening and propensities for TCP phase formation, a guideline regarding the optimum lattice misfit for future alloy design may be provided by this comparison.

As well-known from literature, the accumulation of a significant amount of primary creep strain is attributed to shearing by stacking fault ribbons in the LTHS regime.[45–48] The nucleation and propagation of these stacking fault ribbons requires exceeding a threshold stress,[48,49] which is approximately 530 MPa at 750 °C for CMSX-4.[48] This threshold stress is significantly increased for Ru-containing 4th generation Ni-base superalloys as shearing by stacking fault ribbons is still inhibited at creep conditions of 750 °C and 750 to 800 MPa.[31,50,51] The absence of significant primary creep strain in these superalloys is explained by the dissociation of a/2 ⟨110⟩ dislocations in the vertical γ matrix channels, which reduces the dislocation mobility and the frequency of the required dislocation reactions to nucleate the stacking fault ribbons.[31,50,51] Whether a dislocation with the Burgers vector b completely separates into two partial dislocations, depends on the stacking fault energy (SFE) of the matrix χ and the acting misfit stress σ_m as follows[52]:

$$\sigma_{min}^{[001]} = \frac{6\sqrt{6}}{b}\chi + \sigma_m, \qquad [4]$$

where $\sigma_{min}^{[001]}$ is the necessary minimum applied stress along the [001] direction at which the dislocation completely separates. Thus, both a more negative lattice misfit and a lower stacking fault energy of the matrix phase promote the dissociation of the dislocations in the matrix phase. Interestingly, dislocations are observed to be dissociated in the vertical γ matrix channels, while they are still undissociated in the horizontal γ matrix channels.[31,50] Due to the different stress states in the vertical and horizontal γ channels and the constant stacking fault energy, these microstructural defect observations highlight the importance of the lattice misfit in the dissociation of the dislocations and thus the improvement of the creep strength in the LTHS regime. While further carefully designed studies are required to rationalize the isolated influence of the SFE and the lattice misfit, the comparison of the measured lattice misfits and the time for 1 pct plastic creep strain strongly indicates that there exists a threshold lattice misfit of about $|\delta| \sim 0.52$ pct for the LDSX alloy series at the creep conditions of 750 °C/800 MPa, above which primary creep is impeded, as shown in Figure 8(a). The increase in creep strength for even higher lattice misfit values (up to − 1.3 pct) is not significant and most likely related to the differences in the chemical composition of the alloys.

Conversely, lower lattice misfit values correlate to higher creep strengths in the ITIS regime (see Figure 8(b)). Since 950 °C is only slightly above the aging temperature, the formation of pronounced interfacial dislocation networks, which relieve the misfit stresses, is expected to occur during the creep experiment and not during the heating-up stage. Thus, it is apparent that the deviation of LDSX-3 from the fitted line is a result of the already present interfacial dislocation networks and the associated incoherence. Since creep deformation in this regime is considered to prevail in the γ channels at lower creep strains, higher lattice misfits should induce coherency stresses that act opposite to the applied tensile load in the vertical γ channels and thus improve the creep properties. However, based on our results this effect does not appear to be dominant as the creep strength increases with decreasing misfit magnitude. Carroll et al. also analyzed the creep behavior of several Ru-containing superalloys and found that the alloys with the highest lattice misfit do not necessarily have the highest creep resistance.[53] While microstructural degradation processes are negligible during creep in the LTHS regime, their role is significantly increased under ITIS conditions. By increasing the coarsening rates and facilitating rafting, higher lattice misfit values lead to a faster degradation of the microstructure and thus to worse creep properties. Even though rafting is often considered to be a strengthening mechanism, this is only the case if the applied stress is low enough to prohibit shearing of the γ' rafts, which is not the case for intermediate stress level.[54–56] Besides, TCP phases can already form in the Mo-rich alloys LDSX-2, -3, -7 and -8 at these temperatures, which would also deteriorate the creep properties.

In the HTLS regime, there appears to be an optimal lattice misfit value of approximately − 0.39 pct at 1100 °C, as shown in Figure 8(c). Investigations by Zhang et al.[5,6] revealed that the interfacial dislocation spacing is proportional to the minimum creep rate in this creep regime. These authors concluded that a higher lattice misfit, which causes a denser interfacial network, impedes shearing processes and thus improves the creep properties. Similarly, the creep properties of the LDSX alloys improve with increasing lattice misfit and thus denser interfacial dislocation networks until $|\delta| \sim 0.39$ pct. While the model of Svoboda and Lukáš[8] predicts that smaller lattice misfit values lead to slightly better creep properties in the HTLS regime, their model does not consider the beneficial aspect of dense interfacial dislocation networks in impeding dislocation slip in the γ' precipitates/rafts. An alloy design program developed by Harada et al.,[57] which classifies the creep rupture strength and temperature capability based on regression analysis, also found that a more negative lattice misfit leads to a higher temperature capability and thus to a higher creep strength in the HTLS regime. These authors, however, noted that in practice a too high lattice misfit value leads to a deterioration of the microstructure and the creep properties. This prediction is confirmed by our in situ aging experiments, which revealed that the coherency stresses for alloys with a
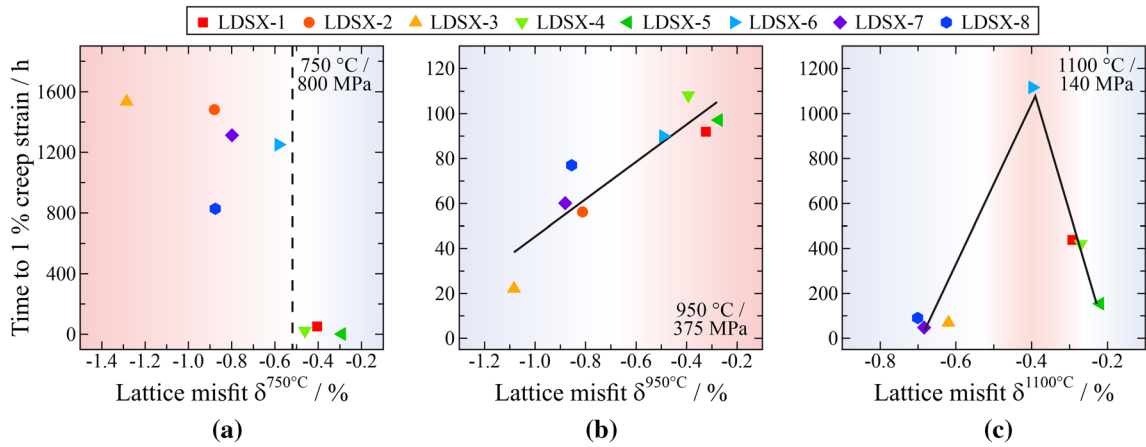
Fig. 8—Correlation between the lattice misfit at the respective temperature and the time to reach 1 pct creep strain at (*a*) 750 °C/800 MPa, (*b*) 950 °C/375 MPa and (*c*) 1100 °C/140 MPa.

higher lattice misfit are completely relieved in the first few hours of the creep experiments. In contrast to alloys with a lower lattice misfit, the relief of the coherency stress during the heating phase and in the initial deformation phase impedes the formation of regular rafts, which are known to improve the creep strength during the first few percent plastic strain in the HTLS regime.[11,54,56,58–61] This microstructural degradation process in combination with the susceptibility to TCP formation explains the diminishing creep strength for alloys with a lattice misfit more negative than 0.39 pct at 1100 °C. Even though this study investigates the influence of the lattice misfit on the creep strength of superalloys with similar γ' volume fractions and precipitate sizes, the optimal precipitate size is also misfit dependent. As shown by Nathal,[42] smaller precipitates ($d \sim 100$ nm) lead to superior creep properties in high lattice misfit alloys ($|\delta| > 0.5$ pct) during high temperature creep. Additionally, the effect of the TCP phase formation in the Mo-rich alloys LDSX-2, -3, -7 and -8 at high temperatures superimposes on the effect of the lattice misfit and therefore it is still unclear whether the optimum lattice misfit magnitude in the HTLS regime is above 0.39 pct. Thus, further work is required to study the optimal lattice misfit in superalloys, which have optimal misfit dependent precipitate sizes and show no TCP phase formation. In summary, the creep properties improve with increasing lattice misfit magnitude in the HTLS regime due to the formation of denser interfacial dislocation networks, which impede shearing of the γ' rafts. However, if the lattice misfit magnitude becomes too large or the content of TCP phase forming elements is too high, microstructural degradation processes during the first one to two hours of the creep experiment or even the heating phase deteriorate the microstructural stability and lead to a decrease of the creep properties.

In typical 1st and 2nd generation Ni-base superalloys, the lattice misfit is close to 0 and becomes more negative with increasing temperature. Even though a lower lattice misfit in the ITIS regime in combination with an optimized misfit in the HTLS regime can be achieved, the lattice misfit is also close to 0 in the LTHS regime,

which leads to significant amounts of primary creep strain. If the Re and Ru contents in 4th generation Ni-base superalloys are high enough (greater than 4 at. pct), the misfit changes atypically with increasing temperature and becomes less negative, as in the case of the LDSX series.[14] However, the lattice misfit can still be only optimized for the LTHS and HTLS regime as its magnitude is too large for the ITIS regime. Similarly, Ni-base and Co-base superalloys with a positive lattice misfit, which gets closer to zero at higher temperatures, can only simultaneously fulfill the optimized misfit values in the LTHS and HTLS regime. Thus, it is unfortunately impossible to achieve optimized lattice misfit magnitudes for all three creep regimes simultaneously.

V. SUMMARY AND CONCLUSION

The microstructural evolution of a series of highly alloyed Ru-containing 4th generation Ni-base superalloys, the LDSX alloy series, was investigated by *in situ* heating and aging X-ray diffraction experiments. Subsequently, the determined lattice misfit values were correlated to previous tensile creep experiments. From this study, the following conclusions can be drawn:

1. The lattice misfits of the LDSX series range between -0.3 and -1.3 pct at room temperature. With increasing temperature, the lattice misfit magnitudes become atypically smaller, whereby the decrease is proportional to the magnitude of the lattice misfit at room temperature. This is mainly due to the partial dissolution of the γ' phase and in some cases additionally due to TCP phase formation.
2. The temporal evolution of the γ sub-peak position and shape at 1100 °C reveals the occurrence of TCP formation and coherency stress relaxation as the γ sub-peak shifts to lower lattice parameters and becomes more symmetrical, respectively.
3. The acting coherency stresses are significantly decreased after aging for 3 hours at 1100 °C. In

LDSX-6 ($\delta^{1100\,^\circ C} = -0.39$ pct), they are relaxed from 280 MPa to a plateau-like region of 85 MPa, while they are completely relieved in the alloys LDSX-3 and LDSX-8, which have a more negative lattice misfit of -0.62 and -0.68 pct at 1100 °C, respectively.

4. While the lattice misfit remains approximately constant for LDSX-6 during the *in situ* aging experiments at 1100 °C, the lattice misfit magnitudes of LDSX-3 and LDSX-8, which are prone to TCP formation, decrease due to the increasing shift of the γ sub-peak to lower lattice parameters.

5. In all three relevant creep regimes, the creep strength depends strongly on the lattice misfit: In the low temperature/high stress regime (750 °C/ 800 MPa), the lattice misfit magnitude should be large enough to inhibit the accumulation of significant amounts of primary creep strain. It should exceed the threshold of 0.52 pct for the LDSX series. In contrast, the lattice misfit magnitude should be as small as possible in the intermediate temperature and stress regime (900 °C/400 MPa). At high temperature and low stresses (1100 °C/ 140 MPa), the lattice misfit magnitude should range around 0.39 pct.

CONFLICT OF INTEREST

On behalf of all authors, the corresponding author states that there is no conflict of interest.

REFERENCES

1. J.S. Van Sluytman and T.M. Pollock: *Acta Mater.*, 2012, vol. 60, pp. 1771–83. https://doi.org/10.1016/j.actamat.2011.12.008.
2. K.A. Christofidou, N.G. Jones, E.J. Pickering, R. Flacau, M.C. Hardy, and H.J. Stone: *J. Alloys Compd.*, 2016, vol. 688, pp. 542–52. https://doi.org/10.1016/j.jallcom.2016.07.159.
3. H. Mughrabi: *Acta Mater.*, 2014, vol. 81, pp. 21–29. https://doi.org/10.1016/j.actamat.2014.08.005.
4. R.C. Reed: *Camb. Core.*, 2006, https://doi.org/10.1017/CBO9780511541285.
5. J.X. Zhang, T. Murakumo, H. Harada, and Y. Koizumi: *Scripta Mater.*, 2003, vol. 48, pp. 287–93. https://doi.org/10.1016/S1359-6462(02)00379-2.
6. J. Zhang, J. Wang, H. Harada, and Y. Koizumi: *Acta Mater.*, 2005, vol. 53, pp. 4623–33. https://doi.org/10.1016/j.actamat.2005.06.013.
7. R. Giraud, Z. Hervier, J. Cormier, G. Saint-Martin, F. Hamon, X. Milhet, and J. Mendez: *Metall. Mater. Trans. A*, 2013, vol. 44A, pp. 131–46. https://doi.org/10.1007/s11661-012-1397-9.
8. J. Svoboda and P. Lukáš: *Acta Mater.*, 1998, vol. 46, pp. 3421–31. https://doi.org/10.1016/S1359-6454(98)00043-3.
9. F. Pyczak, B. Devirent, and H. Mughrabi: in *Superalloys 2004 Tenth Int. Symp.*, TMS, 2004, pp. 827–36. https://doi.org/10.7449/2004/Superalloys_2004_827_836.
10. L. Mueller, T. Link, and M. Feller-kniepmeier: *Scripta Metall. Mater.*, 1992, https://doi.org/10.1016/0956-716X(92)90580-8.
11. F. Xue, C.H. Zenk, L.P. Freund, M. Hoelzel, S. Neumeier, and M. Göken: *Scripta Mater.*, 2018, vol. 142, pp. 129–32. https://doi.org/10.1016/j.scriptamat.2017.08.039.
12. K. Tanaka, M. Ooshima, N. Tsuno, A. Sato, and H. Inui: *Philos. Mag.*, 2012, vol. 92, pp. 4011–27. https://doi.org/10.1080/14786435.2012.700416.
13. F. Diologent, P. Caron, T. d'Almeida, S. Chambreland, A. Jacques, and P. Bastie: *Int. J. Mater. Res.*, 2006, vol. 97, pp. 1136–42. https://doi.org/10.3139/146.101350.
14. S. Neumeier, F. Pyczak, and M. Göken: *Mater. Des.*, 2021, vol. 198, p. 109362. https://doi.org/10.1016/j.matdes.2020.109362.
15. A.C. Yeh, C.M.F. Rae, and S. Tin: in *Superalloys 2004 Tenth Int. Symp.*, TMS, 2004, pp. 677–85. https://doi.org/10.7449/2004/Superalloys_2004_677_685.
16. A. Sato, H. Harada, T. Yokokawa, T. Murakumo, Y. Koizumi, T. Kobayashi, and H. Imai: *Scripta Mater.*, 2006, vol. 54, pp. 1679–84. https://doi.org/10.1016/j.scriptamat.2006.01.003.
17. A. Heckl, S. Neumeier, S. Cenanovic, M. Göken, and R.F. Singer: *Acta Mater.*, 2011, vol. 59, pp. 6563–73. https://doi.org/10.1016/j.actamat.2011.07.002.
18. K. Matuszewski, R. Rettig, H. Matysiak, Z. Peng, I. Povstugar, P. Choi, J. Müller, D. Raabe, E. Spiecker, K.J. Kurzydłowski, and R.F. Singer: *Acta Mater.*, 2015, vol. 95, pp. 274–83. https://doi.org/10.1016/j.actamat.2015.05.033.
19. R.A. Hobbs, L. Zhang, C.M.F. Rae, and S. Tin: *Metall. Mater. Trans. A*, 2008, vol. 39A, pp. 1014–25. https://doi.org/10.1007/s11661-008-9490-9.
20. A.C. Yeh and S. Tin: *Metall. Mater. Trans. A*, 2006, vol. 37A, pp. 2621–31. https://doi.org/10.1007/BF02586097.
21. H.T. Pang, R.A. Hobbs, H.J. Stone, and C.M.F. Rae: *Adv. Mater. Res.*, 2011, vol. 278, pp. 54–59. https://doi.org/10.4028/www.scientific.net/AMR.278.54.
22. T. Sugui, W. Minggang, L. Tang, Q. Benjiang, and X. Jun: *Mater. Sci. Eng. A*, 2010, vol. 527, pp. 5444–51. https://doi.org/10.1016/j.msea.2010.05.027.

23. A. Volek, R.F. Singer, R. Buergel, J. Grossmann, and Y. Wang: *Metall. Mater. Trans. A*, 2006, vol. 37A, pp. 405–10. https://doi.org/10.1007/s11661-006-0011-4.
24. L. Wang, S. Wang, X. Song, Y. Liu, and G. Xu: *Int. J. Fatigue*, 2014, vol. 62, pp. 210–16. https://doi.org/10.1016/j.ijfatigue.2013.10.006.
25. Z. Zhang and Z. Yue: *J. Alloys Compd.*, 2018, vol. 746, pp. 84–92. https://doi.org/10.1016/j.jallcom.2018.02.133.
26. H.-A. Kuhn, H. Biermann, T. Ungár, and H. Mughrabi: *Acta Metall. Mater.*, 1991, vol. 39, pp. 2783–94. https://doi.org/10.1016/0956-7151(91)90095-I.
27. F. Pyczak, S. Neumeier, and M. Göken: *Mater. Sci. Eng. A*, 2009, vol. 510–511, pp. 295–300. https://doi.org/10.1016/j.msea.2008.08.052.
28. H. Biermann, M. Strehler, and H. Mughrabi: *Scripta Metall. Mater.*, 1995, vol. 32, pp. 1405–10. https://doi.org/10.1016/0956-716X(95)00179-Y.
29. T. Link, A. Epishin, U. Brückner, and P. Portella: *Acta Mater.*, 2000, vol. 48, pp. 1981–94. https://doi.org/10.1016/S1359-6454(99)00456-5.
30. A. Jacques and P. Bastie: *Philos. Mag.*, 2003, vol. 83, pp. 3005–27. https://doi.org/10.1080/1478643031000149108.
31. R.A. Hobbs, G.J. Brewster, C.M.F. Rae, and S. Tin: in *Superalloys 2008 Elev. Int. Symp.*, TMS, 2008, pp. 171–80 https://doi.org/10.7449/2008/Superalloys_2008_171_180.
32. C.A. Schneider, W.S. Rasband, and K.W. Eliceiri: *Nat. Methods.*, 2012, vol. 9, pp. 671–75. https://doi.org/10.1038/nmeth.2089.
33. S. Giese, A. Bezold, M. Pröbstle, A. Heckl, S. Neumeier, and M. Göken: *Metall. Mater. Trans. A*, 2020, https://doi.org/10.1007/s11661-020-06028-0.
34. M. Wilkens and K. Eckert: *Z. Für Naturforschung A*, 1964, https://doi.org/10.1515/zna-1964-0410.
35. C.H. Zenk, S. Neumeier, H.J. Stone, and M. Göken: *Intermetallics*, 2014, vol. 55, pp. 28–39. https://doi.org/10.1016/j.intermet.2014.07.006.
36. D. Siebörger, H. Knake, and U. Glatzel: *Mater. Sci. Eng. A*, 2001, vol. 298, pp. 26–33. https://doi.org/10.1016/S0921-5093(00)01318-6.
37. C. Schulze and M. Feller-Kniepmeier: *Mater. Sci. Eng. A*, 2000, vol. 281, pp. 204–12. https://doi.org/10.1016/S0921-5093(99)00713-3.
38. R. Völkl, U. Glatzel, and M. Feller-Kniepmeier: *Acta Mater.*, 1998, vol. 46, pp. 4395–4404. https://doi.org/10.1016/S1359-6454(98)00085-8.
39. U. Brückner, A. Epishin, T. Link, and K. Dressel: *Mater. Sci. Eng. A*, 1998, vol. 247, pp. 23–31. https://doi.org/10.1016/S0921-5093(97)00856-3.
40. S. Neumeier, J. Ang, R.A. Hobbs, C.M.F. Rae, and H.J. Stone: *Adv. Mater. Res.*, 2011, vol. 278, pp. 60–65. https://doi.org/10.4028/www.scientific.net/AMR.278.60.
41. C.J. Smithells: *Metals Reference Book*, Elsevier Science, Kent, 2014. http://qut.eblib.com.au/patron/FullRecord.aspx?p=1839022. Accessed 26 April 2020.
42. M.V. Nathal: *Metall. Trans. A*, 1987, vol. 18A, pp. 1961–70. https://doi.org/10.1007/BF02647026.
43. T. Murakumo, T. Kobayashi, Y. Koizumi, and H. Harada: *Acta Mater.*, 2004, vol. 52, pp. 3737–44. https://doi.org/10.1016/j.actamat.2004.04.028.
44. S. Neumeier, F. Pyczak, and M. Göken: in *Superalloys 2008 Elev. Int. Symp.*, TMS, 2008, pp. 109–19. https://doi.org/10.7449/2008/Superalloys_2008_109_119.
45. G.R. Leverant and B.H. Kear: *Metall. Mater. Trans. B*, 1970, vol. 1, pp. 491–98. https://doi.org/10.1007/BF02811560.
46. G.R. Leverant, B.H. Kear, and J.M. Oblak: *Metall. Trans.*, 1973, vol. 4, pp. 355–62. https://doi.org/10.1007/BF02649637.
47. C.M.F. Rae, N. Matan, and R.C. Reed: *Mater. Sci. Eng. A*, 2001, vol. 300, pp. 125–34. https://doi.org/10.1016/S0921-5093(00)01788-3.
48. C.M.F. Rae and R.C. Reed: *Acta Mater.*, 2007, vol. 55, pp. 1067–81. https://doi.org/10.1016/j.actamat.2006.09.026.
49. V. Sass, U. Glatzel, and M. Feller-Kniepmeier: *Acta Mater.*, 1996, vol. 44, pp. 1967–77. https://doi.org/10.1016/1359-6454(95)00315-0.
50. N. Tsuno, K. Kakehi, C.M.F. Rae, and R. Hashizume: *Metall. Mater. Trans. A*, 2009, vol. 40A, pp. 269–72. https://doi.org/10.1007/s11661-008-9744-6.
51. S. Shimabayashi and K. Kakehi: *Scripta Mater.*, 2010, vol. 63, pp. 909–12. https://doi.org/10.1016/j.scriptamat.2010.06.048.
52. S. Ma, L. Carroll, and T.M. Pollock: *Acta Mater.*, 2007, vol. 58, pp. 5802–12.
53. L.J. Carroll, Q. Feng, and T.M. Pollock: *Metall. Mater. Trans. A*, 2008, vol. 39A, pp. 1290–1307. https://doi.org/10.1007/s11661-008-9520-7.
54. H. Mughrabi, W. Schneider, V. Sass, and C. Lang: *Strength Mater. ICSMA*, 1994, vol. 10, pp. 705–08.
55. P. Caron, P.J. Henderson, T. Khan, and M. McLean: *Scripta Metall.*, 1986, vol. 20, pp. 875–80. https://doi.org/10.1016/0036-9748(86)90458-8.
56. R.C. Reed, N. Matan, D.C. Cox, M.A. Rist, and C.M.F. Rae: *Acta Mater.*, 1999, vol. 47, pp. 3367–81. https://doi.org/10.1016/S1359-6454(99)00217-7.
57. H. Harada, T. Yamagata, T. Yokokawa, K. Ohno, and M. Yamazaki: in *Proc 5Th Int Conf Creep Fract. Eng. Mater. Struct.*, IOM, London, UK, 1993, pp. 255–64.
58. D.D. Pearson, B.H. Kear, and F.D. Lemkey: in *Creep Fract.*, Pineridge Press, Swansea, 1981, p. 213.
59. P. Caron and T. Khan: *Mater. Sci. Eng.*, 1983, vol. 61, pp. 173–84. https://doi.org/10.1016/0025-5416(83)90199-4.
60. R.A. MacKay and L.J. Ebert: *Metall. Trans. A*, 1985, vol. 16A, pp. 1969–82. https://doi.org/10.1007/BF02662398.
61. F.R.N. Nabarro: *Metall. Mater. Trans. A*, 1996, vol. 27A, pp. 513–30. https://doi.org/10.1007/BF02648942.